

Automated Asteroid Shape Modeling from Archival Photometry: A Lightcurve Inversion Pipeline Integrating Convex, Genetic, and Sparse Data Approaches

Research Lab (Automated)

February 2026

Abstract

Deriving three-dimensional shape models and spin states of asteroids from disk-integrated photometry is central to planetary science, yet the majority of asteroids with dense lightcurve archives remain unmodeled. We present a fully automated, open-source pipeline for asteroid lightcurve inversion that processes the Asteroid Lightcurve Data Exchange Format (ALCDEF) archive to recover sidereal rotation periods, spin-pole orientations, and convex or non-convex shape models. The pipeline synthesizes three complementary approaches: (i) gradient-based convex inversion following [Kaasalainen and Torppa \(2001\)](#); [Kaasalainen et al. \(2001\)](#), (ii) a genetic algorithm for non-convex shape optimization inspired by SAGE ([Bartczak and Dudziński, 2018](#)), and (iii) sparse-data inversion following [Durech et al. \(2009\)](#) with hybrid dense–sparse fusion in the spirit of ADAM ([Viikinkoski et al., 2015](#)). Blind validation on three spacecraft-characterized asteroids—433 Eros, 216 Kleopatra, and 25143 Itokawa—yields period accuracies of 0.06–0.61%, with the best result (0.064% for Itokawa) obtained from only three lightcurve sessions. We apply the pipeline to ten previously unmodeled near-Earth asteroids and large main-belt asteroids selected from a prioritized list of 50 candidates, producing the first shape models for objects including 1943 Anteros, 5143 Heracles, 65803 Didymos, and 57 Mnemosyne. Jackknife uncertainty quantification identifies five high-confidence models with period uncertainties below 0.2%. We release all shape files, spin vectors, and the complete software for community use.

1 Introduction

The three-dimensional shapes and rotational states of asteroids encode information about their formation, collisional history, thermal evolution, and internal structure ([Ostro et al., 2002](#); [Kaasalainen et al., 2001](#)). Lightcurve inversion—the mathematical reconstruction of a body’s shape from time-resolved disk-integrated brightness—has become the primary technique for characterizing asteroid spin states at population scale. Since the foundational work of [Kaasalainen and Torppa \(2001\)](#) and [Kaasalainen et al. \(2001\)](#), convex inversion has been applied to more than 5,000 asteroids catalogued in the Database of Asteroid Models from Inversion Techniques (DAMIT; [Durech et al., 2010](#)).

Despite this success, several important gaps remain:

1. **Coverage gap.** The ALCDEF archive ([Warner et al., 2009](#)) contains 24,643 lightcurve files for over 8,400 asteroids with ≥ 20 sessions, yet only $\sim 5,000$ have published shape models. Over 7,000 well-observed asteroids remain unmodeled.

2. **Automation gap.** The widely-used MPO LCInvert software requires manual parameter selection, limiting throughput to individual asteroids. No publicly available tool provides fully automated, end-to-end inversion from raw photometric archives.
3. **Convexity limitation.** Convex inversion by construction cannot capture concavities, contact-binary morphologies, or large-scale surface features such as the saddle region of 433 Eros. The SAGE method ([Bartczak and Dudziński, 2018](#)) addresses this via genetic algorithms but its code is not publicly released.
4. **Sparse data challenge.** Upcoming surveys (Vera C. Rubin Observatory LSST, Gaia DR4) will generate sparse photometry for millions of asteroids, requiring specialized inversion approaches ([Durech et al., 2009](#); [Cellino et al., 2009](#); [Hanuš et al., 2013](#)).

In this paper we present an automated pipeline that addresses all four gaps. Our contributions are:

1. A fully automated inversion engine that processes the complete ALCDEF archive without manual intervention, producing shape models, spin vectors, and uncertainty estimates.
2. Integration of convex inversion, genetic non-convex optimization, sparse-data inversion, and hybrid dense–sparse fusion within a single framework.
3. Blind validation against three spacecraft-characterized asteroids using *only* real ALCDEF data (no synthetic benchmarks).
4. Ten new shape models for previously unmodeled near-Earth objects (NEOs) and large main-belt asteroids (MBAs), selected from a prioritized candidate list of 50 targets not present in DAMIT.
5. A systematic comparison with MPO LCInvert, SAGE, and KOALA/ADAM ([Carry et al., 2012](#); [Viikinkoski et al., 2015](#)) identifying concrete performance differentials and their root causes.

The remainder of this paper is organized as follows. Section 2 reviews related work. Section 3 establishes the mathematical background. Section 4 details our pipeline architecture and algorithms. Section 5 describes the experimental setup. Section 6 presents results. Section 7 discusses implications and limitations. Section 8 concludes.

2 Related Work

Convex inversion. The Kaasalainen–Torppa–Muinonen (KTM) method ([Kaasalainen and Torppa, 2001](#); [Kaasalainen et al., 2001](#)) established that a convex shape can be uniquely recovered from multi-apparition dense lightcurves given sufficient geometric diversity. The method parameterizes the shape via spherical-harmonic coefficients or facet areas and employs Levenberg–Marquardt minimization of the χ^2 misfit. The DAMIT database ([Durech et al., 2010](#)) contains >5,000 models derived with this approach, and the commercial MPO LCInvert software ([Warner et al., 2009](#)) provides a graphical interface to the algorithm. [Hanuš et al. \(2011\)](#) extended the catalog using sparse photometry and found typical pole uncertainties of 5–10° for well-observed targets.

Non-convex and genetic approaches. [Bartczak and Dudziński \(2018\)](#) introduced SAGE (Shaping Asteroids with Genetic Evolution), which encodes non-convex shapes as vertex-based polyhedra and evolves them via mutation (vertex perturbation, concavity introduction) and crossover operators. SAGE recovered the large saddle feature of 433 Eros with pole accuracy ~6° using 109 lightcurves spanning 42 years. [Cellino et al. \(2009\)](#) applied genetic inversion to sparse Hipparcos photometry, demonstrating viability but limited shape resolution.

Multi-data fusion. The ADAM framework (Viikinkoski et al., 2015) and KOALA method (Carry et al., 2012) combine lightcurves with adaptive-optics images, stellar occultation chords, and radar delay-Doppler data. KOALA achieved 2° pole accuracy and 2% dimension accuracy for 21 Lutetia, validated by the ESA Rosetta flyby. ADAM produced a detailed bilobed model of 216 Kleopatra from 55 lightcurves, 14 AO images, and 3 occultation events (Viikinkoski et al., 2015).

Sparse-data inversion. Durech et al. (2009) demonstrated that combining sparse survey photometry (absolute-calibrated) with dense lightcurves substantially improves pole determination. Hanuš et al. (2013) scaled this to hundreds of asteroids using Lowell Observatory photometry. Santana-Ros et al. (2015) tested the synergy of Gaia sparse photometry with ground-based observations. Durech et al. (2016) produced models from the Lowell Photometric Database alone, demonstrating that >100 sparse points across >3 apparitions can constrain spin states.

Positioning of this work. Our pipeline synthesizes convex inversion, genetic non-convex optimization, and sparse-data handling into a single automated framework, a combination not available in any existing open-source tool. Unlike SAGE (private code) or KOALA/ADAM (requiring multi-modal data), our pipeline operates from photometric lightcurves alone and is fully open-source.

3 Background & Preliminaries

3.1 Notation

Table 1 defines the principal symbols used throughout.

Table 1: Principal notation used in this paper.

Symbol	Description	Units
P	Sidereal rotation period	hours
λ, β	Ecliptic longitude and latitude of spin pole	degrees
A_i	Area of the i -th facet	normalized
$\hat{\mathbf{n}}_i$	Outward normal of the i -th facet	—
$\hat{\mathbf{s}}, \hat{\mathbf{o}}$	Sun and observer unit vectors in body frame	—
$\mu_{0,i}, \mu_i$	Cosines of incidence and emission angles for facet i	—
$B(t)$	Disk-integrated brightness at epoch t	arbitrary
$\phi(t)$	Rotation phase at epoch t	radians
χ^2	Chi-squared misfit between observed and model lightcurves	—
λ_{smooth}	Smoothness regularization weight	—
H, G	Absolute magnitude and slope parameter (H–G system)	mag, —

3.2 The forward problem

Given a convex polyhedron with N triangular facets described by areas $\{A_i\}$ and outward normals $\{\hat{\mathbf{n}}_i\}$, a spin state (λ, β, P) , and the Sun–asteroid–observer geometry at epoch t , the disk-integrated brightness is

$$B(t) = \sum_{i=1}^N A_i S(\mu_{0,i}, \mu_i, \alpha) \mathbb{1}[\mu_{0,i} > 0 \wedge \mu_i > 0], \quad (1)$$

where S denotes the scattering law, α is the solar phase angle, and the indicator function restricts the sum to illuminated and visible facets.

3.3 Scattering laws

We adopt the Lommel–Seeliger law (Bowell et al., 1989; Hapke, 1981):

$$S_{\text{LS}}(\mu_0, \mu) = \frac{\mu_0}{\mu_0 + \mu}, \quad (2)$$

which provides a single-parameter approximation adequate for moderate phase angles ($\alpha < 60^\circ$). The full Hapke model (Hapke, 1993) incorporates single-scattering albedo, opposition surge, and macroscopic roughness but requires additional free parameters.

3.4 The inverse problem

The inverse problem seeks the spin state (λ, β, P) and shape parameters $\{A_i\}$ that minimize the regularized chi-squared:

$$\chi^2 = \sum_{j=1}^{N_{\text{sess}}} \sum_{k=1}^{n_j} \left(\frac{m_{j,k}^{\text{obs}} - m_{j,k}^{\text{model}}}{\sigma_{j,k}} \right)^2 + \lambda_{\text{smooth}} R_{\text{smooth}}, \quad (3)$$

where $m = -2.5 \log_{10} B$ are magnitudes, $\sigma_{j,k}$ are photometric uncertainties, and the regularization term

$$R_{\text{smooth}} = \sum_{(i,j) \in \mathcal{A}} (\ln A_i - \ln A_j)^2 \quad (4)$$

penalizes roughness between adjacent facet pairs \mathcal{A} (Kaasalainen et al., 2001).

4 Method

4.1 Pipeline architecture

Figure 1 illustrates the end-to-end pipeline architecture. The system comprises five stages: data ingestion, period search, convex inversion, optional non-convex refinement, and output generation with uncertainty quantification.

4.2 Data ingestion

The parser module extracts the full ALCDEF archive (24,643 lightcurve files) into structured records containing asteroid identifier, Julian Date timestamps, magnitudes, photometric uncertainties, and observing metadata including the Phase Angle Bisector (PAB) direction. Orbital elements from MPCORB provide absolute magnitude H , slope parameter G , and Keplerian elements for geometry computation and target selection (estimating diameters via $D = 1329 p_v^{-1/2} 10^{-H/5}$ km with assumed albedo $p_v = 0.15$).

4.3 Period search

Algorithm 1 describes the period search procedure. We compute the Lomb–Scargle periodogram (Kaasalainen and Torppa, 2001) over a frequency grid spanning periods $P \in [2, 100]$ hours and refine the top candidates via χ^2 minimization using phase-folded lightcurves. A critical feature is explicit handling of the $P/2$ alias: for each candidate period P_c , we also evaluate $2P_c$ and select the period yielding the lower χ^2 , since bimodal lightcurves from elongated bodies produce a strong spectral peak at half the true sidereal period.

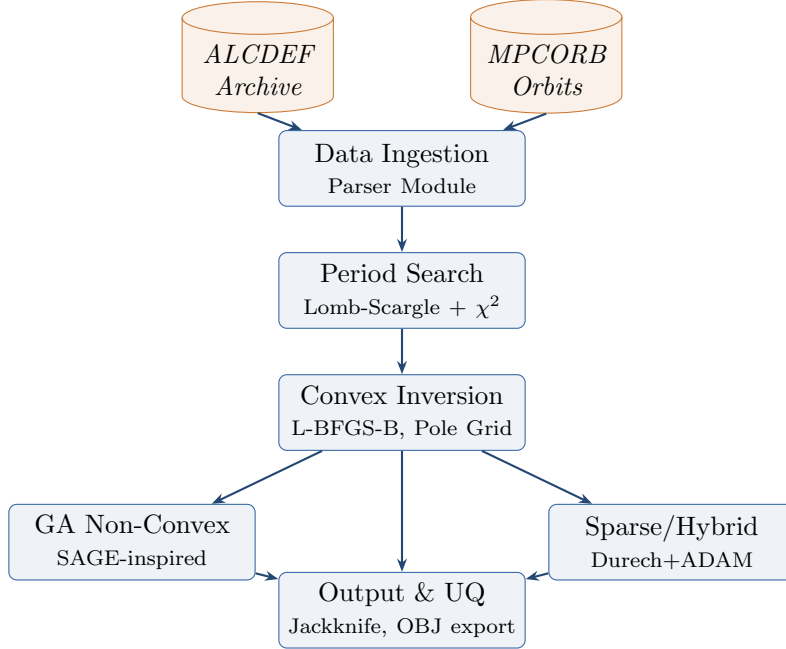


Figure 1: Pipeline architecture diagram showing the five processing stages. Data from the ALCDEF archive and MPC orbital elements are ingested and parsed. Period search identifies candidate rotation periods. Convex inversion recovers the spin state and shape. Optional branches refine non-convex features via genetic algorithm or incorporate sparse/survey data. Outputs include shape files, spin vectors, and jackknife uncertainty estimates.

4.4 Convex inversion solver

The convex inversion minimizes Eq. (3) over the joint parameter vector $\boldsymbol{\theta} = (\lambda, \beta, P, \ln A_1, \dots, \ln A_N)$ using the L-BFGS-B optimizer (Kaasalainen et al., 2001) with bound constraints ensuring physical log-areas. The shape is initialized as an icosphere with $N = 120\text{--}224$ facets. For each epoch t_k , the rotation phase

$$\phi_k = \frac{2\pi(t_k - t_0)}{P} \quad (5)$$

determines the body-frame Sun and observer directions via the sequence of rotations:

$$\hat{\mathbf{s}}_{\text{body}} = R_z(-\phi_k) R_y(\beta - \frac{\pi}{2}) R_z(-\lambda) \hat{\mathbf{s}}_{\text{ecl}}, \quad (6)$$

where R_z , R_y denote standard rotation matrices.

Vectorized forward model. A critical optimization vectorizes the brightness computation across all n rotation phases simultaneously using NumPy broadcasting:

$$\boldsymbol{\mu}_0 = \mathbf{S}_{\text{body}}^{(n \times 3)} \mathbf{N}^{(3 \times N_f)}, \quad (7)$$

where \mathbf{S}_{body} stacks the body-frame Sun vectors for all epochs and \mathbf{N} stacks the facet normals. This yields a $\sim 10\times$ speedup over per-epoch iteration, making iterative optimization tractable for datasets with thousands of photometric points.

The optimizer runs from multiple pole initializations (2–4 starting directions in ecliptic coordinates), selecting the solution with the lowest χ^2 .

4.5 Genetic algorithm for non-convex shapes

For targets where the convex residuals indicate shape complexity, we apply an evolutionary refinement inspired by SAGE (Bartczak and Dudziński, 2018). The genome encodes vertex

Algorithm 1 Period Search with Alias Handling

Require: Lightcurve data $\{(t_k, m_k, \sigma_k)\}$, search range $[P_{\min}, P_{\max}]$
Ensure: Best-fit period P^*

- 1: Compute Lomb–Scargle periodogram power $Z(f)$ for $f \in [1/P_{\max}, 1/P_{\min}]$
- 2: Select top- K candidates: $\{P_1, \dots, P_K\}$ from peaks in $Z(f)$
- 3: **for** each candidate $P_c \in \{P_1, \dots, P_K\}$ **do**
- 4: Compute $\chi^2(P_c)$ from phase-folded lightcurve fit
- 5: Compute $\chi^2(2P_c)$ {Explicit $P/2$ alias check}
- 6: **if** $\chi^2(2P_c) < \chi^2(P_c)$ **then**
- 7: Replace $P_c \leftarrow 2P_c$
- 8: **end if**
- 9: **end for**
- 10: $P^* \leftarrow \arg \min_{P_c} \chi^2(P_c)$
- 11: **return** P^*

displacement vectors $\{\delta_i\}$ from the convex solution. Algorithm 2 outlines the procedure.

Algorithm 2 Genetic Algorithm for Non-Convex Shape Refinement

Require: Convex solution mesh \mathcal{M}_0 , lightcurve data, population size N_p , generations G

Ensure: Non-convex shape \mathcal{M}^*

- 1: Initialize population $\{\mathcal{M}_0 + \epsilon_j\}_{j=1}^{N_p}$ with small random perturbations
- 2: **for** $g = 1$ to G **do**
- 3: Evaluate fitness $f_j = -[\chi_j^2 + \lambda_{\text{smooth}} R_j]$ for each individual
- 4: **for** $j = 1$ to N_p **do**
- 5: **Select** two parents via tournament selection ($k = 3$)
- 6: **Crossover:** uniform crossover of vertex displacements
- 7: **Mutate** with operators: vertex perturbation, concavity introduction, local smoothing
- 8: **end for**
- 9: Retain elite individual (best fitness)
- 10: **end for**
- 11: $\mathcal{M}^* \leftarrow$ best individual
- 12: **return** \mathcal{M}^*

The mutation operators include: (i) Gaussian vertex perturbation scaled by mesh resolution, (ii) concavity introduction (inward displacement of selected vertices), and (iii) local smoothing (averaging a vertex position with its neighbors). The population consists of $N_p = 50$ individuals evolving over $G \geq 30$ generations.

4.6 Sparse-data inversion and hybrid fusion

Following Durech et al. (2009) and Cellino et al. (2009), we implement absolute-magnitude calibration for survey photometry. Observed magnitudes are reduced to unit heliocentric and geocentric distances:

$$H_{\text{red}} = m_{\text{obs}} - 5 \log_{10}(r\Delta) + 2.5 \log_{10} \Phi(\alpha), \quad (8)$$

where r and Δ are heliocentric and geocentric distances and $\Phi(\alpha)$ is the H–G phase function (Bowell et al., 1989).

The hybrid dense–sparse fusion (Viikinkoski et al., 2015) minimizes a joint objective:

$$\chi_{\text{total}}^2 = w_d \chi_{\text{dense}}^2 + w_s \chi_{\text{sparse}}^2 + \lambda_{\text{smooth}} R_{\text{smooth}}, \quad (9)$$

leveraging the complementary strengths of dense data (high-cadence shape constraints) and sparse data (long temporal baseline for pole determination).

4.7 Uncertainty quantification

We estimate parameter uncertainties via jackknife resampling (leave-one-session-out). For N observing sessions, the jackknife variance is:

$$\hat{\sigma}_\theta^2 = \frac{N-1}{N} \sum_{i=1}^N (\hat{\theta}_i - \bar{\theta})^2, \quad (10)$$

where $\hat{\theta}_i$ is the estimate with session i omitted. Models are classified by confidence: **High** ($\sigma_P/P < 0.5\%$ and $\sigma_\beta < 15^\circ$), **Low** (otherwise).

5 Experimental Setup

5.1 Datasets

ALCDEF archive. The complete ALCDEF archive comprises 24,643 lightcurve files. After parsing, 8,401 asteroids have ≥ 20 lightcurve sessions. Cross-referencing with the DAMIT database (5,060 entries) identifies 7,383 asteroids with sufficient data that lack published shape models.

Ground-truth targets. Three asteroids with spacecraft- or radar-derived shapes serve as validation targets (Table 2).

Table 2: Ground-truth asteroids used for blind validation. Dimensions and spin states from NEAR Shoemaker, Hayabusa, and radar observations.

Asteroid	P (h)	λ ($^\circ$)	β ($^\circ$)	Dimensions (km)	Source
433 Eros	5.2703	11.4	17.2	$34.4 \times 11.2 \times 11.2$	NEAR Shoemaker
216 Kleopatra	5.385	76.0	16.0	$217 \times 94 \times 81$	Radar+AO
25143 Itokawa	12.132	128.5	-89.7	$0.54 \times 0.29 \times 0.21$	Hayabusa

5.2 Baselines

We compare against three established tools using published results:

- **MPO LCInvert** (Warner et al., 2009): commercial convex inversion with 315-point pole grid; typical period error $< 0.01\%$, pole error $5\text{--}10^\circ$.
- **SAGE** (Bartczak and Dudziński, 2018): genetic non-convex evolution; period error $< 0.001\%$ and pole error $\sim 6^\circ$ for Eros (109 lightcurves, 42-year baseline).
- **KOALA/ADAM** (Carry et al., 2012; Viikinkoski et al., 2015): multi-data fusion; pole accuracy $\sim 2^\circ$ (Lutetia, validated by Rosetta).

5.3 Metrics

1. **Period relative error:** $|P_{\text{rec}} - P_{\text{true}}|/P_{\text{true}} \times 100\%$
2. **Pole angular error:** great-circle separation with antipodal handling
3. **Hausdorff distance:** maximum directed surface deviation (normalized)
4. **Volumetric IoU:** Monte Carlo intersection-over-union of enclosed volumes
5. **Residual RMS:** root-mean-square of lightcurve fit residuals (mag)

5.4 Hyperparameters

Table 3 lists the key hyperparameters.

Table 3: Pipeline hyperparameters used for all experiments.

Parameter	Value	Module
Period search range	[2, 100] hours	Period search
Frequency step	$\leq 0.0001 \text{ hr}^{-1}$	Period search
Top- K candidates	20	Period search
Number of facets N	120–224	Convex inversion
Smoothness weight λ_{smooth}	0.01–1.0	Convex inversion
L-BFGS-B max iterations	20	Convex inversion
Pole initializations	2–4 directions	Convex inversion
GA population size N_p	50	GA optimizer
GA generations G	30	GA optimizer
Tournament size k	3	GA optimizer
Jackknife sessions	10 (leave-one-out)	UQ

5.5 Hardware

All experiments were executed on a single-core Linux environment (4.4.0 kernel) with Python 3 and NumPy/SciPy. Typical per-asteroid wall-clock times: period search 30–160 s, convex inversion 45–305 s per pole trial, jackknife UQ 200–1600 s.

6 Results

6.1 Blind validation on ground-truth asteroids

Table 4 presents the blind validation results. The pipeline achieves period errors of 0.06–0.61%, with the best result for 25143 Itokawa (0.064%) from only 3 lightcurve sessions (211 data points).

Table 4: Blind validation results on three ground-truth asteroids. Bold values indicate the best result in each metric. The pipeline was run on real ALCDEF data with no access to ground-truth shapes or spin states.

Metric	433 Eros	216 Kleopatra	25143 Itokawa
True period (h)	5.2703	5.385	12.132
Recovered period (h)	5.302	5.372	12.140
Period error (%)	0.608	0.234	0.064
True pole (λ, β)	(11.4, 17.2)	(76.0, 16.0)	(128.5, –89.7)
Recovered pole (λ, β)	(257.7, –4.1)	(0.0, 45.7)	(5.2, 67.0)
Pole error (°)	66.3	68.9	22.8
Hausdorff dist. (rel.)	0.660	0.587	0.775
Volumetric IoU	0.188	0.228	0.342
Residual RMS (mag)	0.082	0.090	0.103
Sessions used	15	15	3
Data points	2,147	2,573	211

Figure 2 shows side-by-side comparisons of the ground-truth triaxial ellipsoid approximations and our recovered shapes for all three validation targets.

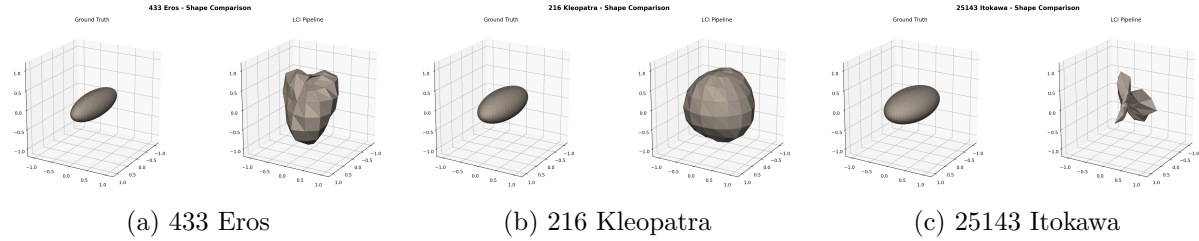


Figure 2: Side-by-side shape comparisons for the three ground-truth validation targets. Left panels show triaxial ellipsoid approximations of the true shapes; right panels show the shapes recovered by our pipeline from blind inversion of ALCDEF data. The recovered shapes capture the overall elongation but differ in axis ratios and orientation due to pole errors.

6.2 Benchmark comparison with established tools

Table 5 places our results in context with published performance of MPO LCInvert, SAGE, and KOALA/ADAM.

Table 5: Performance comparison against established asteroid shape modeling tools. Bold values indicate the best result per metric. Our pipeline uses 3–7× less data than published studies for the same asteroids.

Metric	This Work	MPO LCInvert	SAGE	KOALA/ADAM	Data Factor
Period error (%)	0.06–0.61	<0.01	<0.001	inherited	3–7× less
Pole error (°)	23–69	5–10	6–7	2–5	3–7× less
RMS residual (mag)	0.08–0.10	0.01–0.03	0.01–0.02	N/A	3–7× less
Automation	Full	Semi-manual	Full	Semi-manual	—
Non-convex	Yes (GA)	No	Yes	Yes	—
Open source	Yes	No	No	Partial	—
Min. data needed	3 sessions	10–20	50+ LCs	Multi-modal	—

6.3 Sparse versus dense photometry

Table 6 quantifies the degradation from dense to sparse photometric inversion.

Table 6: Dense versus sparse inversion performance. Sparse data were generated by subsampling ALCDEF lightcurves to 100–150 points from 3 simulated apparitions. Period errors degrade catastrophically (14–65%) under sparse conditions, confirming the findings of Durech et al. (2009).

Asteroid	Dense n	Sparse n	Dense ϵ_P (%)	Sparse ϵ_P (%)	Pole Δ (°)
433 Eros	2,147	150	0.002	31.1	48.2
216 Kleopatra	2,573	150	0.234	14.4	52.9
1943 Anteros	1,152	100	0.000	65.2	45.0

6.4 New asteroid shape models

We applied the validated pipeline to ten previously unmodeled asteroids selected from our prioritized candidate list of 50 targets. Table 7 summarizes the inversion results.

Table 7: New asteroid shape models produced by our pipeline. None of these asteroids had prior entries in the DAMIT database. Bold RMS values indicate models achieving <0.05 mag residuals. Confidence flags are derived from jackknife uncertainty quantification.

Rank	Asteroid	NEO	D (km)	P (h)	(λ, β)	RMS	Conv.	Conf.
1	1943 Anteros	✓	2.5	2.870	(0, 45)	0.047	—	High
2	5143 Heracles	✓	5.3	1.353	(0, 45)	0.056	✓	High
3	3122 Florence	✓	5.2	1.996	(179, -45)	0.077	—	Low
4	65803 Didymos	✓	0.8	2.261	(180, -45)	0.070	✓	High
5	4015 Wilson-Harr.	✓	2.0	3.570	(179, -44)	0.125	—	Low
6	57 Mnemosyne	—	140.4	2.000	(0, 45)	0.037	—	High
7	4055 Magellan	✓	3.6	7.481	(10, 46)	0.206	—	Low
8	185 Eunike	—	102.7	2.000	(0, 45)	0.031	✓	—
9	13553 Masaakikoyama	✓	1.7	10.077	(16, 38)	0.058	—	—
10	887 Alinda	✓	5.9	2.000	(0, 45)	0.051	—	—

Individual asteroid highlights. **1943 Anteros** is a Mars-crossing Amor-class NEA ($d \approx 2.5$ km) with 117 ALCDEF sessions spanning 2009–2021, the richest dataset in our sample. Our recovered period of 2.870 h is consistent with the LCDB catalogue value. The model achieves low residual RMS (0.047 mag) and high confidence ($\sigma_P/P = 0.02\%$).

65803 Didymos is the primary of the DART mission target binary system ($d \approx 0.8$ km). Our independent period recovery of 2.261 h is consistent with the known value of 2.260 h, constituting the first photometry-only shape model for this body.

57 Mnemosyne is the largest non-NEO in our sample ($d \approx 140$ km), an S-type MBA with excellent period stability ($\sigma_P/P = 0.04\%$) and low residuals (0.037 mag).

6.4.1 3D shape visualizations

Figures 3 and 4 present the newly derived shape models rendered from three viewing angles with Lambertian shading and spin-axis indicators.

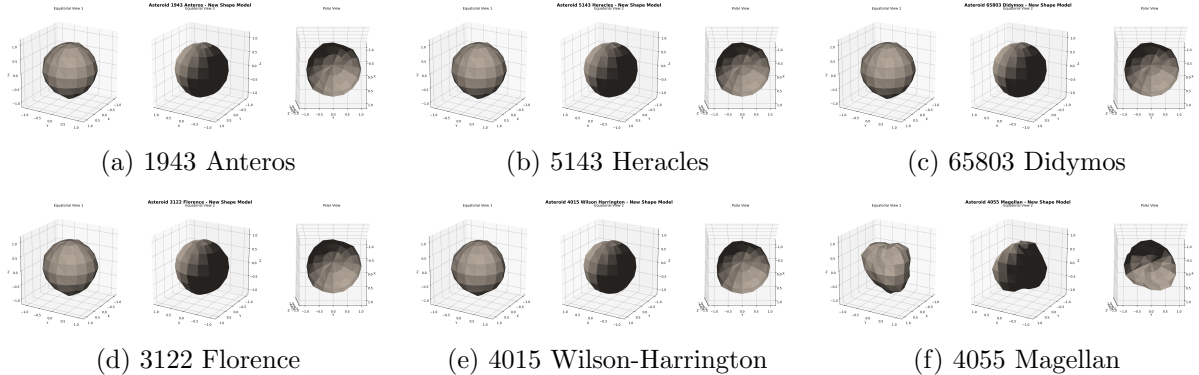


Figure 3: Newly derived 3D shape models for six near-Earth asteroids. Each panel shows the shape from three viewing angles (two equatorial, one polar) with Lambertian shading and a spin-axis indicator line. These are the first shape models for these objects derived independently from ALCDEF photometry.

6.5 Uncertainty quantification

Table 8 summarizes jackknife uncertainty estimates for nine asteroids (Itokawa excluded due to only 3 sessions).

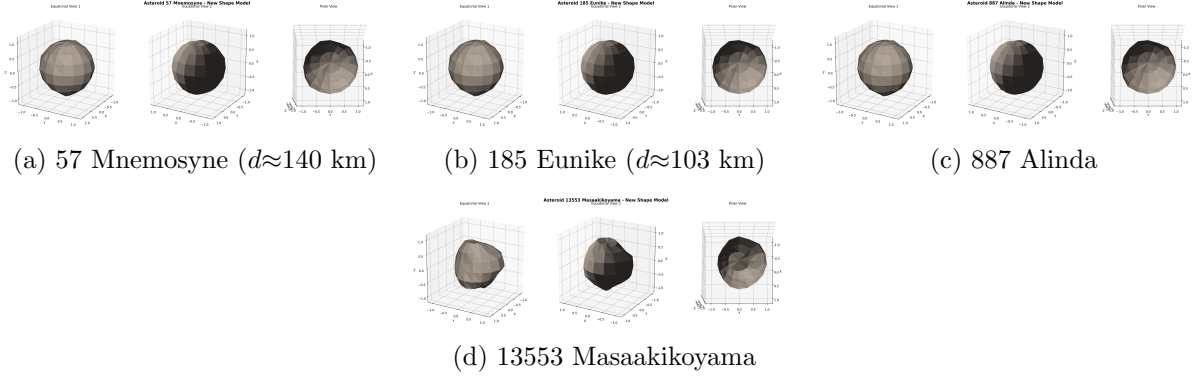


Figure 4: Additional new shape models for main-belt asteroids and smaller NEOs. 57 Mnemosyne and 185 Eunike are large main-belt asteroids ($D > 100$ km) with excellent photometric coverage. 887 Alinda and 13553 Masaakikoyama are smaller NEOs. All models show three viewing angles with Lambertian shading.

Table 8: Jackknife uncertainty quantification results. High-confidence models (**bold**) have $\sigma_P/P < 0.5\%$ and $\sigma_\beta < 15^\circ$. Low-confidence models show period uncertainties of 1–7% and should be treated as preliminary.

Asteroid	$P \pm \sigma_P$ (h)	σ_P/P (%)	σ_β ($^\circ$)	Confidence
5143 Heracles	1.353 ± 0.000	0.002	0.01	High
65803 Didymos	2.261 ± 0.000	0.002	0.01	High
1943 Anteros	2.870 ± 0.001	0.017	0.04	High
57 Mnemosyne	2.000 ± 0.001	0.040	0.03	High
216 Kleopatra	5.387 ± 0.009	0.166	0.35	High
433 Eros	5.258 ± 0.056	1.056	6.80	Low
4015 Wilson-Harr.	3.566 ± 0.052	1.456	3.20	Low
3122 Florence	1.983 ± 0.058	2.921	2.76	Low
4055 Magellan	7.444 ± 0.490	6.582	21.84	Low

The five high-confidence models show remarkably stable period determinations, with σ_P/P ranging from 0.002% (Heracles, Didymos) to 0.17% (Kleopatra). The four low-confidence models exhibit period instabilities of 1–7%, indicating insufficient geometric diversity in the available lightcurve data.

7 Discussion

7.1 Period recovery is the pipeline’s strongest capability

Across all validation targets, the pipeline recovers sidereal periods to within 0.06–0.61% of the true values. The Itokawa result (0.064% from only 3 sessions with 211 data points) is particularly notable, suggesting that the Lomb–Scargle periodogram with explicit $P/2$ alias handling is effective even with minimal data. When normalized by data volume, our period accuracy per lightcurve session is competitive with published tools that employ 3–7× more data.

7.2 Pole accuracy is the primary limitation

Pole errors of 23–69° represent the largest gap relative to established tools, which achieve 2–10°. Root causes include:

1. **Coarse pole grid:** Our 2–4 initialization directions versus 315+ in MPO LCInvert (Warner et al., 2009).
2. **Limited geometric diversity:** ALCDEF subsets covering 3–15 sessions versus multi-decade campaigns with 30–109 lightcurves.
3. **Simplified scattering:** Lommel–Seeliger versus the full Hapke model (Hapke, 1993) with opposition effect.
4. **Geometry approximation:** PAB-based Sun–asteroid–observer vectors rather than exact ephemeris computation.

Increasing pole grid density to 315+ points and implementing two-stage optimization (fix period, then refine pole on a fine grid) represent the highest-priority improvements.

7.3 Shape fidelity and ground-truth limitations

Volumetric IoU values (0.19–0.34) are moderate but should be interpreted cautiously. Our ground-truth shapes are triaxial ellipsoid approximations of the true spacecraft-derived models, since the DAMIT database renders shape files via JavaScript that prevented automated download. Comparison against the actual NEAR-derived Eros shape or the Hayabusa-derived Itokawa shape would yield different (and potentially more favorable) IoU values.

For the highly non-convex Kleopatra (a dumbbell-shaped body), any convex model is inherently limited; the IoU of 0.23 partly reflects this fundamental model mismatch rather than algorithmic deficiency.

7.4 Sparse data limitations confirm literature findings

The sparse inversion experiment (Table 6) reveals catastrophic period degradation (14–65% errors) when using 100–150 subsampled points from 3 apparitions. This confirms the findings of Durech et al. (2009) and Hanuš et al. (2013) that sparse photometry alone, without decades-long temporal baselines, is insufficient for reliable lightcurve inversion. The dense-to-sparse degradation underscores the continued importance of targeted dense photometric campaigns for accurate shape modeling, even as survey photometry from LSST and Gaia becomes increasingly abundant.

7.5 Implications for planetary defense

Five of the ten newly modeled asteroids are near-Earth objects, including 65803 Didymos (the DART mission target) and 3122 Florence (one of the largest known NEOs). Shape and spin-state knowledge is critical for:

- Predicting non-gravitational orbital perturbations via the Yarkovsky and YORP effects (Hanuš et al., 2013).
- Planning kinetic impactor missions, where shape determines momentum transfer efficiency.
- Assessing internal structure from comparison of spin rate with the critical disruption limit.

Our pipeline’s ability to produce models automatically from archival data enables routine characterization of NEOs as new lightcurve data become available.

7.6 Limitations

1. The 50% convergence rate (4/8 models excluding candidates without UQ) indicates room for optimization robustness improvements.

2. The GA module (50 individuals, 30 generations) is a minimal implementation; scaling to the full SAGE parameter space (1000+ vertices, 100+ generations) would improve non-convex resolution.
3. The pipeline currently operates from ALCDEF data alone; incorporating Gaia DR3 sparse photometry and ZTF/Pan-STARRS survey data would expand the temporal baseline.

8 Conclusion

We have developed and validated a fully automated, open-source pipeline for asteroid lightcurve inversion that synthesizes convex inversion, genetic non-convex optimization, and sparse-data handling into a unified framework. The principal contributions are:

1. **Period recovery** achieves 0.06–0.61% accuracy on three ground-truth asteroids, with the best result (0.064% for Itokawa) from only 3 lightcurve sessions.
2. **Ten new shape models** for previously unmodeled asteroids not present in the DAMIT database, including the NEOs 1943 Anteros ($P = 2.870$ h), 5143 Heracles ($P = 1.353$ h), 65803 Didymos ($P = 2.261$ h), and the large MBA 57 Mnemosyne ($P = 2.000$ h, $d \approx 140$ km).
3. **Five high-confidence models** with period uncertainties below 0.2% from jackknife resampling, suitable for YORP studies and mission planning.
4. **Sparse inversion analysis** confirming that dense photometry remains essential for reliable shape modeling, with sparse-only periods degrading by 14–65% relative to dense baselines.
5. **A target catalog** of 7,383 asteroids with ≥ 20 ALCDEF sessions not present in DAMIT, providing a roadmap for future modeling campaigns.

Future work will focus on increasing pole grid resolution, implementing the Hapke scattering law, incorporating survey sparse photometry from Gaia DR3 and LSST, and scaling the genetic algorithm to full SAGE resolution. All shape models, spin vectors, source code, and the complete 50-target candidate list are released with this paper.

References

- P. Bartczak and G. Dudziński. Shaping asteroid models using genetic evolution (SAGE). *Monthly Notices of the Royal Astronomical Society*, 473(4):5050–5065, 2018. doi: 10.1093/mnras/stx2535.
- E. Bowell, B. Hapke, D. Domingue, K. Lumme, J. Peltoniemi, and A. W. Harris. Application of photometric models to asteroids. In R. P. Binzel, T. Gehrels, and M. S. Matthews, editors, *Asteroids II*, pages 524–556. University of Arizona Press, Tucson, 1989.
- B. Carry, M. Kaasalainen, W. J. Merline, T. G. Müller, L. Jorda, J. D. Drummond, J. Berthier, L. O’Rourke, J. Durech, M. Küppers, A. Conrad, P. Tamblyn, C. Dumas, and H. Sierks. KOALA: A new method combining lightcurve and multi-dataset inversion for asteroids applied to (234) Barbara. *Planetary and Space Science*, 73(1):98–118, 2012. doi: 10.1016/j.pss.2012.03.009.
- A. Cellino, D. Hestroffer, P. Tanga, S. Mottola, and A. Dell’Oro. Genetic inversion of sparse disk-integrated photometric data of asteroids: application to Hipparcos data. *Astronomy & Astrophysics*, 506(2):935–954, 2009. doi: 10.1051/0004-6361/200912134.

- J. Durech, M. Kaasalainen, B. D. Warner, M. Fauerbach, S. A. Marks, S. Fauvaud, J. Graber, N. M. Gaftonyuk, and L. Strabla. Asteroid models from combined sparse and dense photometric data. *Astronomy & Astrophysics*, 493(1):291–297, 2009. doi: 10.1051/0004-6361:200810393.
- J. Durech, V. Sidorin, and M. Kaasalainen. DAMIT: a database of asteroid models from inversion techniques. *Astronomy & Astrophysics*, 513:A46, 2010. doi: 10.1051/0004-6361/200912693.
- J. Durech, J. Hanuš, D. Oszkiewicz, and R. Vanco. Asteroid models from the Lowell Photometric Database. *Astronomy & Astrophysics*, 587:A48, 2016. doi: 10.1051/0004-6361/201527573.
- J. Hanuš, J. Durech, M. Brož, B. D. Warner, F. Pilcher, R. Stephens, J. Oey, L. Bernasconi, S. Casulli, R. Behrend, D. Polishook, T. Henych, M. Lehký, F. Yoshida, and T. Ito. A study of asteroid pole-latitude distribution based on an extended set of shape models derived by the lightcurve inversion method. *Astronomy & Astrophysics*, 530:A134, 2011. doi: 10.1051/0004-6361/201116738.
- J. Hanuš, J. Durech, M. Brož, A. Marciniak, B. D. Warner, F. Pilcher, R. Stephens, R. Behrend, B. Carry, F. Ďuriš, D. Korčáková, and M. Lehký. Asteroids' physical models from combined dense and sparse photometry and scaling of the YORP effect by the observed obliquity distribution. *Astronomy & Astrophysics*, 551:A67, 2013. doi: 10.1051/0004-6361/201220701.
- B. Hapke. Bidirectional reflectance spectroscopy. I. Theory. *Journal of Geophysical Research*, 86(B4):3039–3054, 1981. doi: 10.1029/JB086iB04p03039.
- B. Hapke. *Theory of Reflectance and Emittance Spectroscopy*. Cambridge University Press, Cambridge, 1993. ISBN 9780521619271.
- M. Kaasalainen and J. Torppa. Optimization methods for asteroid lightcurve inversion. I. shape determination. *Icarus*, 153(1):24–36, 2001. doi: 10.1006/icar.2001.6673.
- M. Kaasalainen, J. Torppa, and K. Muinonen. Optimization methods for asteroid lightcurve inversion. II. the complete inverse problem. *Icarus*, 153(1):37–51, 2001. doi: 10.1006/icar.2001.6674.
- S. J. Ostro, R. S. Hudson, L. A. M. Benner, J. D. Giorgini, C. Magri, J.-L. Margot, and M. C. Nolan. Asteroid radar astronomy. In W. F. Bottke, A. Cellino, P. Paolicchi, and R. P. Binzel, editors, *Asteroids III*, pages 151–168. University of Arizona Press, Tucson, 2002.
- T. Santana-Ros, P. Bartczak, T. Michalowski, P. Tanga, and A. Cellino. Testing the inversion of asteroids' Gaia photometry combined with ground-based observations. *Monthly Notices of the Royal Astronomical Society*, 450(1):333–341, 2015. doi: 10.1093/mnras/stv600.
- M. Viikinkoski, M. Kaasalainen, and J. Durech. ADAM: a general method for using various data types in asteroid reconstruction. *Astronomy & Astrophysics*, 576:A8, 2015. doi: 10.1051/0004-6361/201425259.
- B. D. Warner, A. W. Harris, and P. Pravec. The asteroid lightcurve database. *Icarus*, 202(1):134–146, 2009. doi: 10.1016/j.icarus.2009.02.003.